ADVANCING EARTH AND SPACE SCIENCES

JGR Planets

RESEARCH ARTICLE

10.1029/2026JE009898

Key Points:

- Young Chang'e-6 and Chang'e-5 basalts both originated from shallow ilmenite-bearing cumulate source
- Upper limit of ilmenite beneath the PKT is ~8 wt% higher than the farside SPA basin
- Higher ilmenite lowers the solidus and leads to large-scale nearside volcanism

Supporting Information:

Supporting Information may be found in the online version of this article.

Correspondence to:

B. Zhang and Y. Qian,
geozhangbo@pku.edu.cn;
yuqiqian@hku.hk

Citation:

Li, Z., Zhang, M., Zhang, B., Qian, Y., Long, T., Che, X., et al. (2026). Asymmetric ilmenite-bearing cumulates triggered lunar dichotomic volcanism on the nearside and farside. *Journal of Geophysical Research: Planets*, *131*, e2026JE009898. https://doi.org/10.1029/2026JE009898

Received 7 MAY 2026
Accepted 11 AUG 2026

Author Contributions:

Conceptualization: Ziqing Li, Bo Zhang, Yuqi Qian, James W. Head
Formal analysis: Ziqing Li, Mengfan Zhang, Yuqi Qian, Tao Long, Xiaochao Che, Ao Su
Funding acquisition: Bo Zhang
Investigation: Ziqing Li, Mengfan Zhang, Yuqi Qian, Tao Long, Xiaochao Che, Ao Su
Methodology: Ziqing Li, Mengfan Zhang, Bo Zhang
Resources: Ziqing Li, Bo Zhang, Ao Su
Visualization: Mengfan Zhang
Writing – original draft: Ziqing Li
Writing – review & editing: Bo Zhang, Yuqi Qian, James W. Head

Asymmetric Ilmenite-Bearing Cumulates Triggered Lunar Dichotomic Volcanism on the Nearside and Farside

Ziqing Li[1], Mengfan Zhang[2], Bo Zhang[1], Yuqi Qian[3], Tao Long[4], Xiaochao Che[4], Ao Su[1], and James W. Head[5]

[1]Key Laboratory of Orogenic Belts and Crustal Evolution, School of Earth and Space Sciences, Peking University, Beijing, China, [2]School of Earth and Space Sciences and Institute of Energy, Peking University, Beijing, China, [3]Department of Earth and Planetary Sciences, NWU-HKU Joint Center of Earth and Planetary Sciences, The University of Hong Kong, Hong Kong, China, [4]Beijing SHRIMP Center, Institute of Geology, Chinese Academy of Geological Sciences, Beijing, China, [5]Department of Earth, Environmental, and Planetary Sciences, Brown University, Providence, RI, USA

Abstract The cause of the observed mare basalt asymmetry between the lunar nearside and farside remains a long-lasting conundrum. In this study, we characterized the petrology and geochemistry of the Chang'e-6 low-Ti basalts from the lunar farside, performed petrological modeling of major elements and conducted Monte Carlo simulation of trace elements, for Chang'e-6 and Chang'e-5 basalts. The results from multiple approaches indicate that the young Chang'e-6 (2.8 Ga) and Chang'e-5 (2.0 Ga) basalts both originated from shallow, depleted ilmenite-bearing cumulate (IBC). Based on remote sensing and thermodynamic constraints, we estimated the mantle source ilmenite abundance for young shallow-source basalts (<3.0 Ga) globally. The modeling results indicate that the mantle sources of these basalts on the nearside generally contains ~16–32 wt% ilmenite, especially beneath the PKT, whereas the mantle sources of these basalts beneath the farside SPA basin only has ~13–24 wt% ilmenite. The phase equilibrium calculations show that the nearside mantle sources with higher ilmenite abundance leads to a significant decrease in melting point and tends to produce more melt compared to farside mantle sources. Therefore, asymmetric IBCs may play a key role in accounting for asymmetric nearside/farside volcanism.

Plain Language Summary The Moon has many more volcanic plains on the side facing Earth than on the farside, but the reason for this difference is still not fully understood. In this study, we examined the rocks returned by the Chang'e-6 mission from the South Pole-Aitken basin on the lunar farside and compared them with young basalts from the Chang'e-5 mission on the nearside. Using mineral chemistry, rock composition, and modeling, we found that both groups of basalts were likely produced from partially melted cumulate in the relatively shallow lunar interior. This cumulate contained iron- and titanium-rich minerals that formed during the final stages of the Moon's early development. Comparison with other geologically young lunar volcanic rocks suggests that the shallow interior beneath the Earth-facing side may contain more of these iron- and titanium-rich materials than the farside. Our calculations indicate that this difference could have allowed rocks beneath the Earth-facing side to melt more readily, helping volcanic activity continue there for longer and cover a larger area. Additional samples from different parts of the Moon will be needed to test and refine this explanation.

1. Introduction

Remote sensing observations have identified distinctive asymmetries between the lunar nearside and farside, which remain a long-lasting conundrum in lunar science. These asymmetries include dichotomies in crustal thickness (Wieczorek et al., 2013), topography (Smith et al., 2010), basalt distribution (Hiesinger et al., 2023; Nelson et al., 2014), and thorium (Th) concentrations (Lawrence et al., 2000; Nelson et al., 2014). Among these features, mare basalts provide a key window into the origin of the lunar nearside-farside dichotomy, while variations in crustal structure, topography, and Th distribution may have contributed to the observed mare basalt asymmetry. The vast majority of mare basalts are distributed on the nearside (approximately 93%), especially in the Procellarum KREEP Terrane (PKT), and very small amounts occur associated with large impact basins on the farside (Head et al., 2023; Qian et al., 2024), mainly in the South Pole-Aitken (SPA) basin (Pasckert et al., 2018; X. Wang et al., 2024). Some studies interpreted the larger basaltic area and volumes on the nearside to be due to a thinner anorthositic crust relative to the farside (Head & Wilson, 1992; Solomon, 1975), which facilitates magma ascent and eruption (Head & Wilson, 2017). However, the lack of abundant mare basalts in the SPA basin with the thinnest crustal thickness (<30 km) indicates that crustal thickness may not be the only factor leading to the volcanism difference (Head & Wilson, 1992, 2017). Alternatively, the analysis of lunar samples (Borg et al., 2004; Meyer et al., 1971) and numerical simulations (Laneuville et al., 2018; Zhang et al., 2022) have led to the suggestion that the mare basalt distribution dichotomy may be controlled by lunar mantle heterogeneity related to highly fractionated products (ur)KREEP and/or ilmenite-bearing cumulate (IBC). The (ur)KREEP reservoir is the late residue of lunar magma ocean (LMO) solidification and is enriched in potassium (K), rare earth elements (REE), and phosphorus (P) (Warren, 1985). The direct (Borg et al., 2004) or indirect radioactive heating (Elardo et al., 2025) or melting point reduction (Elardo et al., 2020) of this reservoir, which is concentrated on the nearside, possibly contributed to the prolonged duration and increased scale of volcanism. However, this hypothesis has been challenged by the recently returned young Chang'e-5 (~2.0 Ga, Che et al., 2021; Q.-L. Li et al., 2021) and Chang'e-6 basalts (~2.8 Ga, Cui et al., 2024; Zhang et al., 2024; Che et al., 2025) as the radioactive Sr-Nd isotope results show that the source regions of these young basalts are rarely affected by KREEP component (Tian et al., 2021; Zong et al., 2022; Z. Wang et al., 2024) or even extremely depleted (Cui et al., 2024; Zhou et al., 2025). In contrast, the sinking of the IBC layer concentrated on the nearside into the deep mantle is considered an effective way to reduce the melting point of the lunar mantle and cause large-scale persistent volcanism (Su et al., 2022; C. Wang et al., 2024, 2025). This driving mechanism was supported to some extent by geodynamic simulations (Zhang et al., 2022) and consistent with the TiO_2 content distribution on the lunar surface observed by remote sensing (Kato et al., 2017; Sato et al., 2017). Nonetheless, the understanding of the different volcanic evolutionary processes on these two opposite hemispheres caused by this mantle compositional heterogeneity is still limited, due to the lack of comparison between nearside and farside samples.

Recently, China's Chang'e-6 mission returned the first lunar farside materials from the South Pole-Aitken (SPA) basin (Figure S1 in Supporting Information S1), which provides a new perspective for comparing the volcanic evolution between lunar nearside and farside and investigating the driving mechanism of mare basalt asymmetry. In this study, we characterized the petrology and geochemistry of the Chang'e-6 basalts and performed petrological modeling of major elements, Monte Carlo modeling of trace elements, and thermodynamic simulations. Then, we compared them with the modeling results of previous nearside Chang'e-5 basalt data. These results from multiple approaches indicate that the Chang'e-6 and Chang'e-5 basalts both originated from partial melting of a shallow IBC. Remote sensing observations and corresponding thermodynamic calculation indicate that the ilmenite abundance in the IBC beneath the farside SPA basin is generally lower than that beneath the nearside PKT. In this case, a higher ilmenite abundance on the nearside contributed to lowering the melting point of the lunar mantle and triggered larger-scale volcanism. These findings offer a crucial foundation for revealing the nature and mechanism of nearside and farside volcanism and the origin of the lunar asymmetry.

2. Materials and Methods

2.1. Chang'e-6 Lunar Samples

The 21 basalt clasts in this study were obtained from two powder samples and 2 basalt clasts one epoxy resin target (CE6C0010YJFM004, CE6C0200, and CE6C0000YJYX021GP01) (A total of 23 basaltic clasts) allocated by China National Space Administration (CNSA). These selected clasts were mounted, polished, carbon-coated, and examined with the scanning electron microscope (SEM, ZEISS MERLIN and QUANTA FEG 650) at the Key Laboratory of Orogenic Belts and Crustal Evolution, School of Earth and Space Sciences, Peking University, Beijing and the Institute of Geology, Chinese Academy of Geological Sciences, Beijing (Figure S2 in Supporting Information S1).

2.2. Major Element Analysis

Major element compositions of pyroxene grains in the basalt clasts were obtained using the JEOL JXA-8230 electron probe microanalysis (EPMA) at the Chengpu Detection Company (Langfang, Hebei, China). The operating conditions were as follows: 15.0 kV accelerating voltage, 20 nA beam current, and 1–5 μm beam size. Peak and background counting times were 10 and 5 s for K and Na, 20 and 10 s for major elements of clinopyroxene (Si, Fe, Al, Mg, and Ca) and plagioclase (Si, Al, and Ca), and 40 and 20 s for other minor elements, respectively. The standards for calibration are jadeite (Si and Na), magnetite (Fe), olivine (Mg), corundum (Al), rutile (Ti), rhodonite (Mn), orthoclase (K), calcite (Ca), and chromite (Cr). ZAF (Z-atomic number, A-absorption and F-fluorescence) calibration procedures were used for reducing matrix effects. Pyroxenes that crystallized in the basalts can record the compositional variations of the equilibrated melts. Based on the empirical pyroxene/basalt Ti partitioning relationship by Robinson et al. (2012) ($D_{TiO2}^{pyroxene\text{-}basalt} = 0.0148 * CaO_{pyroxene} + 0.09$), we have reconstructed the magmatic evolution path of the Chang'e-6 basalts.

The bulk compositions of 18 Chang'e-6 basalt clasts were obtained based on published methods in the study of Chang'-5 basalts (Su et al., 2022; Yuan et al., 2022). All clasts have porphyritic to subophitic textures with abundant mineral grains to ensure that the analysis results are not significantly affected by modal abundance (Figure S2 in Supporting Information S1). The bulk major element compositions of clasts are estimated on the basis of mineral average compositions, density, and modal abundances. Considering the possible zoning of some minerals such as pyroxene, conventional calculation methods may cause significant errors. In this case, we applied a quantitative X-ray mapping method with SEM energy-dispersive spectrometry (EDS; X-Max, Oxford, UK) to determine the bulk major element compositions of the Chang'e-6 basalt clasts at the Key Laboratory of Orogenic Belts and Crustal Evolution, School of Earth and Space Sciences, Peking University, Beijing and the Institute of Geology, Chinese Academy of Geological Sciences, Beijing. The average mineral compositions are obtained by the quantitative EDS mapping method (Yuan et al., 2022). The samples were mapped using a beam current of 4.0 nA and an accelerating voltage of 15 kV. The precision and accuracy are better than 1% and 2%, respectively. All void pixels were subtracted before bulk compositions were normalized to 100%. The average bulk chemistry obtained is identical to the published data within error (Che et al., 2025), which demonstrates the reliability of analysis results. It should be clarified that only the bulk major element compositions used as input for the thermodynamic modeling were taken from the basalt clast data set reported by Che et al. (2025). In contrast, the other data sets presented in this study, including the mineral-scale compositions and isotope analyses, were obtained from the samples analyzed in the present work. Thus, the present study does not simply repeat the previously published clast chemistry, but instead combines previously reported bulk major-element data with newly acquired in situ mineral chemical and isotopic data to support the petrological interpretation and thermodynamic modeling.

2.3. Trace Element Analysis

The trace element analysis of pyroxene in two Chang'e-6 basalt clasts was performed by the Chengyu Detection Company (Langfang, Hebei, China) using laser ablation-inductively coupled plasma mass spectrometry (LA-ICP-MS). The LA-ICP-MS system consisted of a New Wave UP-213 laser ablation unit and an Agilent 7900 mass spectrometer. Helium was used as the carrier gas for aerosol transport in the laser ablation system, while argon was employed as the make-up gas to adjust sensitivity. The two gases were mixed via a T-connector before entering the ICP. The analysis was conducted with a laser beam diameter of 40 μm, a frequency of 10 Hz, and an energy density of approximately 10 J/cm^2 on the sample surface. The ICP-MS analysis operated in peak-hopping mode. Each single-spot laser ablation analysis lasted 80 s, including 20 s for background measurement, 40 s for laser ablation signal acquisition, and 20 s for purging. A set of standard samples was analyzed after every eight sample points. Trace element content was processed using a multi-external standard internal standard calibration method with glass reference materials NIST 610 and NIST 612. Silicon was used as the internal standard element, and its content in the target minerals was pre-determined by electron probe microanalysis. Data processing was completed using GLITTER 4.0 software.

2.4. In Situ Sr Isotope Analysis

Sr isotopic analyses of two representive clasts were performed using a Neptune Plus multi-collector inductively coupled plasma mass spectrometer (MC-ICP-MS; Thermo Fisher Scientific, Bremen, Germany) coupled to a Geolas HD excimer ArF laser ablation system (Coherent, Göttingen, Germany) at Wuhan SampleSolution Analytical Technology Co., Ltd., Hubei, China. The Neptune Plus was equipped with nine F cups fitted with 10^{11} Ω resistors. The collector array spanned from L4 to H3 and was configured to monitor Kr, Rb, Er, Yb, and Sr isotopes. A high-sensitivity X-skimmer cone combined with a Jet sample cone was used to enhance signal intensity. For laser ablation, helium was employed as the carrier gas. During single-spot analyses, the laser spot diameter varied from 60 to 160 μm depending on the Sr signal intensity of the target grain. The pulse repetition rate ranged from 8 to 15 Hz, whereas the laser fluence was maintained at approximately 10 J/cm^2. To evaluate the accuracy of the in situ Sr isotope analytical procedure and the calibration strategy, two natural feldspar megacrysts, YG0440 (albite) and YG4301 (anorthite), were analyzed as unknowns/secondary reference materials.

2.5. Fractional Crystallization Modeling

The PETROLOG program (Danyushevsky & Plechov, 2011) was employed to simulate forward and reverse fractional crystallization processes to reconstruct the Chang'e-6 and Apollo primary magma compositions and to test whether the pyroxene equilibrium melt trend is consistent with fractional crystallization of a basaltic parental melt. All simulations were based on pure fractional crystallization (100%) at a constant pressure. All Fe was treated as Fe^{2+} (FeO) and Fe_2O_3 content in the system was determined by the $Fe^{3+} = 0$. Mineral solution models include olivine (Ford et al., 1983), clinopyroxene (Danyushevsky, 2001), plagioclase (Danyushevsky, 2001), and ilmenite (Nielsen, 1985). Spinel was not included in the fractional crystallization modeling because it is a minor accessory phase (<1 vol%) in the mare basalts considered here. The modeling was instead focused on the volumetrically dominant phases that primarily control the major-element evolution of the magmas. The pressure for near-surface fractionation was set at 1 kbar (approximately 15 km depth). The parameters used in reverse crystallization modeling are consistent with those used in forward crystallization modeling, but it adds minerals back into the melt, causing the composition of the parent melt to descend along the liquidus line.

2.6. Multiphase Saturation Point (MSP) Calculation and P-T Estimation of Cpx-Liquid Thermometer

The pressure and temperature conditions of the MSPs of Chang'e-6 primary magmas and other shallow magmas in the remote sensing observations were obtained by phase equilibrium calculations by the GeoPS program (Xiang & Connolly, 2022). The applied thermodynamic data set is tc-ds634, which was developed for the partial melting of ultramafic rocks in anhydrous systems (K_2O-Na_2O-CaO-FeO-MgO-Al_2O_3-SiO_2-TiO_2-Cr_2O_3) (Tomlinson & Holland, 2021). For Chang'e-6 basalts, near-liquidus phase relations were calculated from 1 to 7 kbar for a wide temperature range. The calculated liquid is saturated with ilmenite at relatively low pressures and with clinopyroxene at high pressures. The intersection of the ilmenite-in and clinopyroxene-in curves defines the MSP.

Clinopyroxene-liquid thermobarometers were applied to constrain the Chang'e-6 magma storage P-T conditions (Neave & Putirka, 2017; Putirka, 2008). To obtain robust clinopyroxene–liquid thermobarometric estimates, a strict equilibrium-screening procedure was applied following the general strategy of Neave and Putirka (2017) and recent lunar applications (Luo et al., 2023). First, clinopyroxene compositions were recalculated on the basis of six oxygens, and analyses with unreasonable cation sums (<3.98 or >4.02) were excluded. Second, analyses with very low Na contents (Jd < 0.002) and low total Al contents (total <0.11) were removed, because such grains may reflect analytical uncertainty or disequilibrium incorporation of Mg and Fe during rapid crystal growth. Third, only relatively early-crystallized high-Mg# clinopyroxenes (Mg# = 60–67) were retained as candidate phases for thermobarometric calculations. Finally, clinopyroxene–liquid equilibrium was further evaluated using both Rhodes-diagram consistency and agreement between observed and predicted clinopyroxene components (e.g., EnFs, DiHd, and CaTs). Only analyses that passed all of the above filters were used for the final P–T calculations. Because these thermobarometers were originally calibrated mainly on terrestrial basaltic systems, their application to lunar Ti-bearing magmas may involve additional uncertainty; therefore, the resulting P-T estimates are treated as first-order constraints rather than exact values. Based on the $Kd_{Fe\text{-}Mg}$ value of clinopyroxene (0.27 ± 0.03) (Putirka, 2008), the high-Mg# (60–67) clinopyroxenes from the Chang'e-6 samples could be crystallized from basaltic magmas with Mg# = ∼29–37. Therefore, the chemical composition of Chang'e-5 basalt with Mg# of 33 could represent a suitable equilibrium liquid. In the Rhodes diagram, all the analysis points used to calculate the P-T conditions fall within the error line of the equilibrium with the host melt. Further, all the predicted calcium Tschermak, enstatite-ferrosilite and diopside-hedenbergite components should fall near the 1:1 line with observed components. The estimated maximum temperature and pressure are close to the MSP.

2.7. Partial Melting Modeling of Lunar Mantle and Phase Equilibrium Calculation

The modeling of partial melting of IBCs with various ilmenite abundance was conducted by pMelts program (Ghiorso et al., 2002) to test whether the major-element characteristics of the shallow-source basalts observed by remote sensing can be approximately reproduced by IBC-related source scenarios. The starting compositions were based on the IBC compositions of Lin et al. (2017), because they are experimentally constrained and have been widely used in subsequent lunar petrological studies. For each calculation, the proportion of ilmenite was varied between 0 and 33 wt%, and the complementary non-ilmenite component of the IBC was proportionally renormalized so that the resulting bulk composition summed to 100 wt%. Thus, the modeled series represents systematic variation in the complete bulk-source composition associated with changing ilmenite abundance. No additional source component was introduced into these IBC-only calculations. A pressure of 4 kbar was adopted to approximate the average pressure corresponding to the modeled IBC depth in Lin et al. (2017), and the oxygen fugacity was fixed at the iron-wüstite buffer (IW). Because the mineral chemistry of lunar ilmenite is compositionally variable and cannot be uniquely constrained using the available remote-sensing bulk-composition data, the modeled ilmenite fraction is interpreted as an effective or apparent modal proportion rather than an exact mineralogical abundance. After obtaining the modeling results, we compared the remote sensing data with the modeling database and fitted the most matching mantle sources based on their composition. Although Astudillo Manosalva and Elardo (2024) reported that pMELTS may not accurately reproduce phase equilibria for Mg-rich lunar compositions. However, the IBC compositions modeled in this study is late-stage cumulate which are not Mg-rich, therefore, this specific limitation is unlikely to directly affect our calculations. We emphasize that pMELTS was originally developed for modeling mantle-related phase relations and partial melting to 3 GPa, with its strongest demonstrated improvements relative to MELTS occurring mainly near 1–2 GPa. It has nevertheless also been applied in recent lunar studies over lower-pressure ranges such as Chang'e-5 basalts (0–15 kbar, Luo et al., 2023) and Mg-suite (0–2 kbar, Elardo & Astudillo Manosalva, 2023). Accordingly, we do not use pMELTS here as a precise thermodynamic inversion tool, but only as a first-order comparative framework.

Phase equilibrium modeling was conducted using the GeoPS program and the data set is the same as that applied in Section 2.6. The input endmembers included nearside IBC upper limit with ~32 wt% ilmenite and farside IBC upper limit with ~24 wt% ilmenite, whose compositions were both obtained from Lin et al. (2017). The pressure was set to 3 kbar to correspond to the depth of the top of IBC in the previous study (Lin et al., 2017). The phase-equilibrium calculations of Ti-bearing system were carried out using the revised thermodynamic framework of Tomlinson and Holland (2021), which includes improvements to Ti-bearing end-members and spinel relations relative to Holland et al. (2018). Although this revision does not fully eliminate the mismatch with experimental results for high-Ti lunar basalts (Astudillo Manosalva & Elardo, 2024), it currently represents the most suitable available first-order framework for evaluating Ti-bearing phase relations in such systems.

2.8. REE Monte Carlo Modeling

After excluding the involvement of enriched KREEP components, we conducted REE Monte Carlo modeling to evaluate the most plausible formation process of Chang'e-6 basalt. The diversity of lunar basalts mainly comes from three aspects: (a) the mixing proportion between late-stage IBC and early-stage Ol-Opx cumulates, (b) the degree of partial melting, and (c) the degree of fractional crystallization (Hallis et al., 2014; Snyder et al., 1992). Therefore, we conducted 50,000 random Monte Carlo simulations using mixing proportion, partial melting degree, and fractional crystallization degree as parameters. In addition, the root mean square error (RMSE) between the fitted results and the actual measured 14 REE in this study was used to evaluate the goodness of fit and all simulations were ranked accordingly but only results with RMSE <0.15 were plotted using color band. For each simulation, the source REE composition was first generated by binary mixing of the Ol-Opx cumulate and IBC endmembers, after which melt REE concentrations were calculated using the batch melting equation and then modified by Rayleigh fractional crystallization. The REE compositions and mineral modal abundances of high-Ti and low-Ti mantle sources are collected from reference (Hallis et al., 2014) and their references. The batch melting was modeled using the following equation: $C_L/C_0 = 1/(D_0 + F * (1-D_0))$, where C_L represents the weight concentration of a trace element in the melt; C_0 is the weight concentration of the trace element in the original cumulate source; F is the melt fraction; and D_0 is the bulk distribution coefficient of the solid phase. The trace element concentrations in the remaining melt, following fractional crystallization, were calculated using the Rayleigh fractionation equation: $C_L/C_0 = (1-F)^{D-1}$, where D is the bulk distribution coefficient (the same as in the batch melting model), F is the mass fraction of crystallized solids, and C_0 and C_L are the element concentrations in the initial and final melt, respectively. In the modeling, the source is represented by a dynamic mixing framework between two compositional endmembers (Ol-Opx cumulate and IBC, Snyder et al., 1992), implemented through continuously varying partition coefficients during the REE Monte Carlo calculations. This treatment is more flexible and geologically more realistic than prescribing a fixed source modal mineralogy, because it allows for transitional source characteristics and better captures the compositional heterogeneity implied by the Chang'e-6 basalts. The bulk partition coefficient for each REE was calculated by modal weighting of the mineral-specific partition coefficients. The REE partition coefficients of minerals include olivine

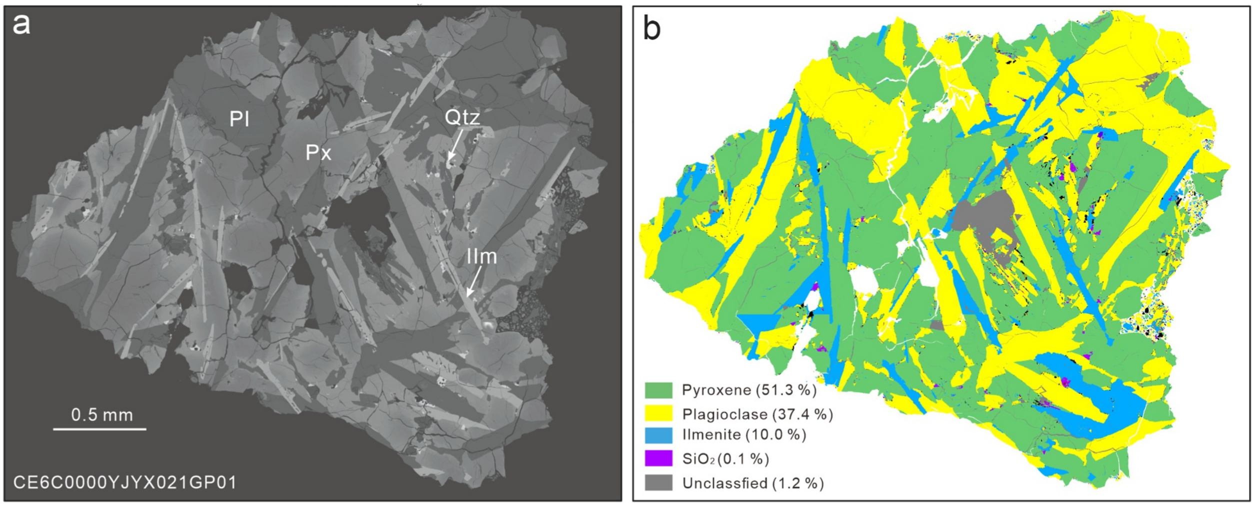

Figure 1. Petrographic observation of Chang'e-6 basalts. (a) Backscattered electron (BSE) image. (b) The EDS analysis results and mineral matching results by Tescan Integrated Mineral Analyzer (TIMA) software.

(McKay, 1986), clinopyroxene (Yao et al., 2012), augite (Yao et al., 2012), pigeonite (McKay et al., 1991), plagioclase (Phinney & Morrison, 1990) and ilmenite (Nakamura et al., 1986).

3. Results

In this study, we chose 23 basaltic clasts from scooped Chang'e-6 lunar soil and used them for petrological observations, mineral composition analyses and bulk composition estimations. Subsequently, large-sized clasts were used for trace element and Sr isotope analysis. The Chang'e-6 basalt clasts are mainly composed of pyroxene, plagioclase, ilmenite and minor amounts of silica, troilite, Ca-phosphates and Zr-bearing minerals (Figure 1; Figure S2 in Supporting Information S1). The mineral abundance modes were estimated to be 45.7–62.2 vol% pyroxene, 34.3–44.7 vol.% plagioclase and 3.3–7.3 vol% ilmenite, with other minerals comprising less than 6 vol.% (Table S1). All clasts are characterized by porphyritic to subophitic textures (heterogeneous mesostasis-rich textures are excluded) and have sizes of >200 μm in order to contain abundant mineral grains in each clast (Figure 1; Figure S2 in Supporting Information S1).

Considering the possible compositional changes in minerals (Che et al., 2025), SEM and EDS quantitative mapping techniques were applied to measure bulk major element compositions of these clasts. The analytical results show that the bulk compositions of Chang'e-6 basalts include 42.1–46.6 wt% SiO_2, 8.3–16.2 wt% Al_2O_3, 16.6–23.6 wt% FeO, 2.7–7.2 wt% MgO, 10.1–12.3 wt% CaO and 1.2–6.7 wt% TiO_2 (Table S1). Generally, the Chang'e-6 basalts have <6 wt% TiO_2 (Table S1) and contain lamellar ilmenite cross-cutting the early pyroxene and plagioclase, which could be defined as a typical low-Ti type (Neal & Taylor, 1992; Papike et al., 1976). Subsequently, we analyzed the mineral composition of the Chang'e-6 basalts using EPMA. The results show that pyroxenes have a composition of $En_{1.0-43.9}Fs_{24.7-79.0}Wo_{13.4-39.6}$ and indicate a cooling crystallization trend of the lava from 1200 to 800°C (Figure S3a in Supporting Information S1 and Table S2). Compared to pyroxenes in the Apollo low-Ti and high-Ti basalts, Chang'e-6 pyroxenes contain lower abundances of enstatite and diopside components. Especially, Chang'e-6 pyroxenes show a rapid decrease in TiO_2 content from ~4.5 to ~1.5 wt% when Mg# value (100*Mg/(Mg + Fe)) decreases from ~65 to ~30 (Figure S3b in Supporting Information S1). The trace element results show that the bulk REE abundance estimated from the most primary pyroxene composition is approximately 20 times higher than chondrite (McDonough & Sun, 1995; Figure S4 in Supporting Information S1 and Table S3). The bulk REE abundance is characterized by a flat pattern with significant negative Eu anomaly (δEu = 0.23), which is consistent with that published in the previous study (Che et al., 2025). The Sr isotope analyses for 14 clean plagioclase grains yielded extremely low initial $^{87}Sr/^{86}Sr$ ratios of 0.699107–0.699310 and the calculated $^{87}Rb/^{86}Sr$ ratios is 0.003–0.010 (Table S4), which are consistent with published values in previous studies (Cui et al., 2024; Zhou et al., 2025).

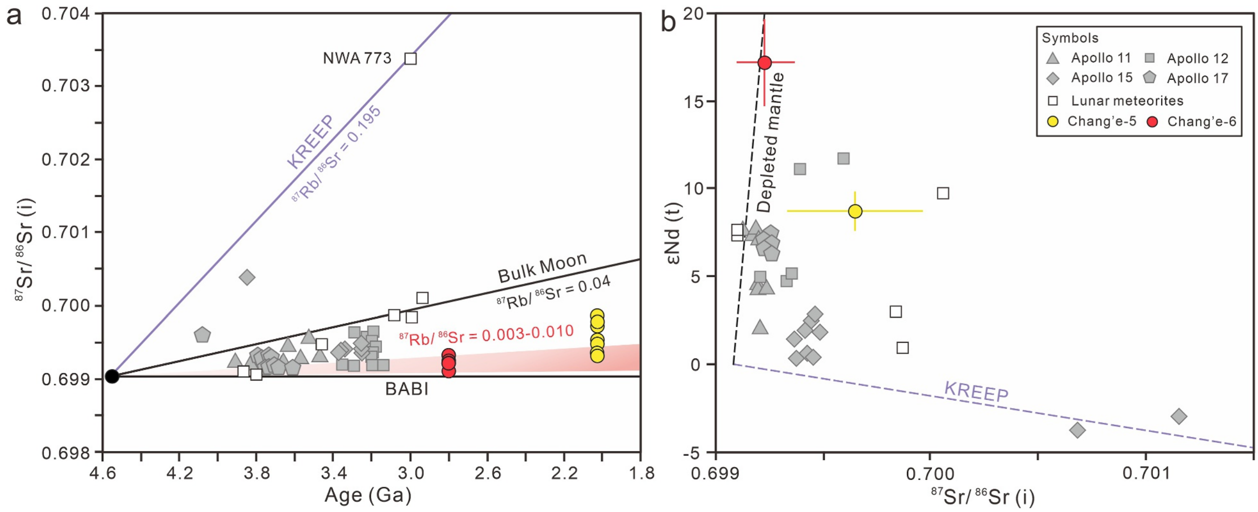

Figure 2. Sr isotopic evolution and Sr-Nd isotope of lunar basalts. (a) $^{87}Sr/^{86}Sr$ ratio evolution of lunar basalts. The $^{87}Rb/^{86}Sr$ ratios of the Chang'e-6 basalt source regions were calculated assuming a single-stage model in which the Moon differentiated at 4.56 Ga, with an initial $^{87}Sr/^{86}Sr$ ratio of 0.69903 (Nyquist, 1977; Nyquist et al., 1973). The initial $^{87}Sr/^{86}Sr$ values were calculated using a rock formation age of 2.807 Ga (Zhang et al., 2024). (b) Initial εNd (t) and initial $^{87}Sr/^{86}Sr$ for lunar basalts. The Chang'e-6 Nd isotope data is from Cui et al. (2024). The Apollo mare basalt and meteorite data are from Elardo et al. (2014) and references therein. The Chang'e-5 basalt data is from Tian et al. (2021). BABI, basaltic achondrite best initial.

4. Discussion

4.1. Young Magmatism From Relatively Depleted Mantle Revealed by Chang'e-6 and Chang'e-5 Basalts

Previous studies have suggested that the mantle sources of lunar mare basalts can be primarily attributed to the mixing of three endmember components, including early-stage cumulates dominated by olivine and orthopyroxene (Ol-Opx), late-stage IBC, and KREEP reservoir from the final crystallization stage of the Lunar Magma Ocean (LMO) (Hallis et al., 2014; Johnson et al., 2021; Longhi, 1992; Snyder et al., 1992). Considering the uncertainty of the mantle source of the Chang'e-6 basalts, radioactive Sr isotope results were first attempted to test whether KREEP components were involved in its mantle source. The low initial $^{87}Sr/^{86}Sr$ ratios of 0.699107–0.699310 and $^{87}Rb/^{86}Sr$ ratios of 0.003–0.010 of the Chang'e-6 basalts suggest a potential depleted mantle source compared to the Apollo KREEP basalts (Figure 2a). Combined with published Nd isotope results (Cui et al., 2024; Zhou et al., 2025), the mantle source of Chang'e-6 basalts can be considered extremely depleted even among all reported mare basalts without enriched KREEP component (Figure 2b). In contrast, the Chang'e-5 basalt is characterized by higher $^{87}Sr/^{86}Sr$ ratios and lower εNd (*t*) values (Tian et al., 2021) compared to the Chang'e-6 basalts, but still far from the KREEP enriched endmember (Figure 2). Based on the previous isotope modeling results (Zong et al., 2022; Z. Wang et al., 2024), this characteristic may suggest a mantle source with 0.5%–1.5% KREEP for the Chang'e-5 basalt rather than a completely depleted source.

4.2. Shallow Ilmenite-Bearing Source Regions of Young Basalts

After determining the involvement from KREEP component to the Chang'e-6 basalts (without KREEP) and Chang'e-5 basalt (~1% KREEP), It is necessary to explore the possible contributions of the other two sources including early-stage Ol-Opx cumulates and late-stage ilmenite-bearing cumulates and determine the pressure-temperature (P-T) conditions of Chang'e-6 magma (Figure 3). The calculated equilibrium melt compositions corresponding to the pyroxene analysis results show that the TiO_2 content in the Chang'e-6 melt first increases and then decreases as Mg# decreases from ~36 to 0. This evolution is consistent with the liquid line of descent independently calculated from the estimated bulk composition (Figure 3a, Figure S5 in Supporting Information S1 and Table S5). Both approaches indicate an initial melt Mg# of only approximately 36, substantially lower than the estimated primary melt compositions of Apollo low-Ti and high-Ti basalts. A similarly low Mg# has also been reported for the Chang'e-5 basalts (Che et al., 2021; Su et al., 2022; Tian et al., 2021).

In this case, a key issue is whether the observed low Mg# value in the Chang'e-6 and Chang'e-5 basalts is the result of fractional crystallization (Su et al., 2022; Tian et al., 2021; Yin et al., 2025) or directly formed through partial

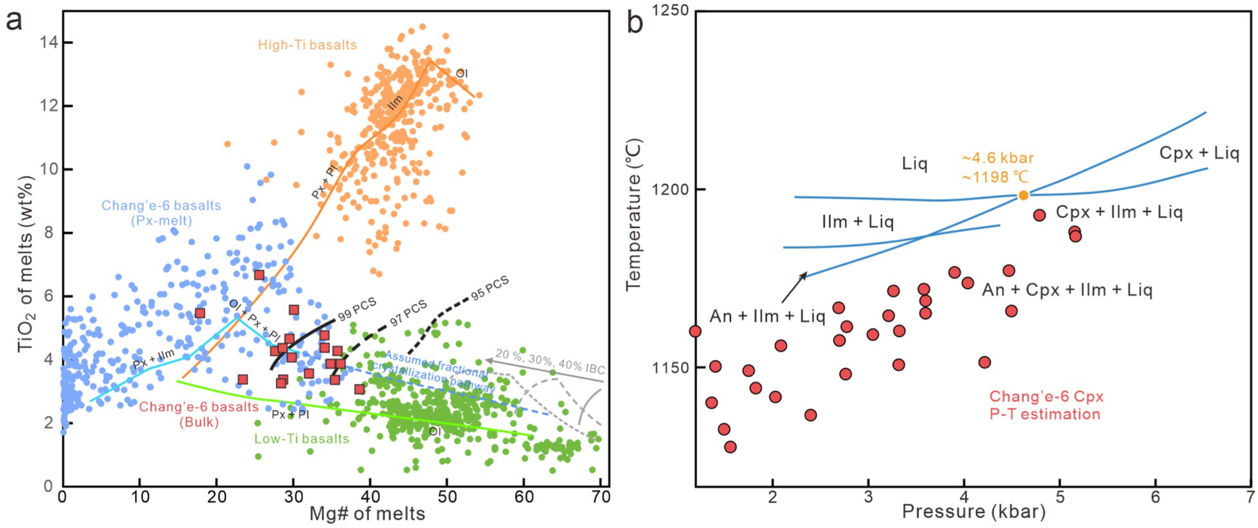

Figure 3. Melt evolution and source region P-T condition estimation of Chang'e-6 low-Ti basalts. (a) Mg# and TiO_2 in the equilibrated melts. The red squares represent bulk compositions based on the EDS analysis. The Apollo low-Ti and high-Ti basalt data is from ApolloBasaltDB_v2 database (Cone, 2021). Fractional crystallization modeling of Chang'e-6 and Apollo basalts was simulated using the PETROLOG program (Danyushevsky & Plechov, 2011). The partial melting modeling of various mantle settings was simulated based on the method in Su et al. (2022) and C. Wang et al. (2024). The hybrid compositions of deep and shallow cumulates are from Johnson et al. (2021) and the 95-99PCS compositions are from Lin et al. (2017). (b) The P-T condition estimation of the multiple saturation point (MSP) and Cpx-liquid thermometer for Chang'e-6 low-Ti basalts.

melting process (C. Wang et al., 2024, 2025), which may indicate different mantle sources. Assuming that the low Mg# value of Chang'e-6 basalts is formed through fractional crystallization, primary magmatic signatures could be progressively reconstituted by the reintroduction of fractionated crystalline mineral phases into the residual melt to drive the melt composition retrograde along the liquid line-of-descent (Section 2; Figure S6 in Supporting Information S1 and Table S6). The Chang'e-6 basalts present a positive correlation between CaO and MgO, indicating that clinopyroxene is an important mineral in the fractionating assemblage (Figure S6 in Supporting Information S1). In contrast, the negative correlation between Al_2O_3 and MgO suggests that plagioclase was not major fractional mineral phase (Figure S6 in Supporting Information S1). Therefore, clinopyroxene was added to the Chang'e-6 basalt first and then followed by olivine in the reverse fractionation modeling process. However, it is uncertain how much clinopyroxene should be added into melt before the appearance of olivine. In this case, we added 10, 20, 30 and 40 mass% clinopyroxene to test transformation in the system. The results show that more than 10 mass% clinopyroxene was required to fit the single trend observed in the Chang'e-6 basalts (Figure S6 in Supporting Information S1). For the case of adding more clinopyroxene with various contents, they lead to slightly different estimations for the primary magma composition, but have little influence on the general fractionation trends (Figure S6 in Supporting Information S1). The addition of olivine is excess but the detailed content will be controlled by mantle melting conditions. The modeling results show that the Chang'e-6 primary melt has a higher TiO_2 content than Apollo low-Ti basalts under similar Mg# values (Figure 3a), suggesting more involvement of late-stage IBC in the Chang'e-6 mantle source than Apollo low-Ti basalts.

Subsequently, we conducted partial melting modeling for a mixed mantle source in different proportions between modeled early-stage Ol-Opx cumulate and late-stage IBC endmembers based on previous study (Su et al., 2022) (Table S7). The modeling results show that the Mg# value in the melt gradually decreases while the TiO_2 content increases as the added IBC proportion increases from 20% to 40% (Figure 3a). However, there are multiple intersections between the melt compositions lines from partial melting and the assumed fractional crystallization trend (Figure 3a). This means that the mantle source of Chang'e-6 will have multiple solutions if the exact degree of fractional crystallization is not known. This controversial issue was also present in studies of the Chang'e-5 basalts (Su et al., 2022; Haupt et al., 2023; C. Wang et al., 2024, 2025), and was relevant to various estimation of their formation depth and temperature-pressure. In fact, previous studies only selected one possibility which considered the most primary Apollo low-Ti basalts (Mg# = ~70) as the standard and ignored other situations (Su et al., 2022; Yin et al., 2025). In contrast, other studies tended to interpret this low Mg# value as direct shallow

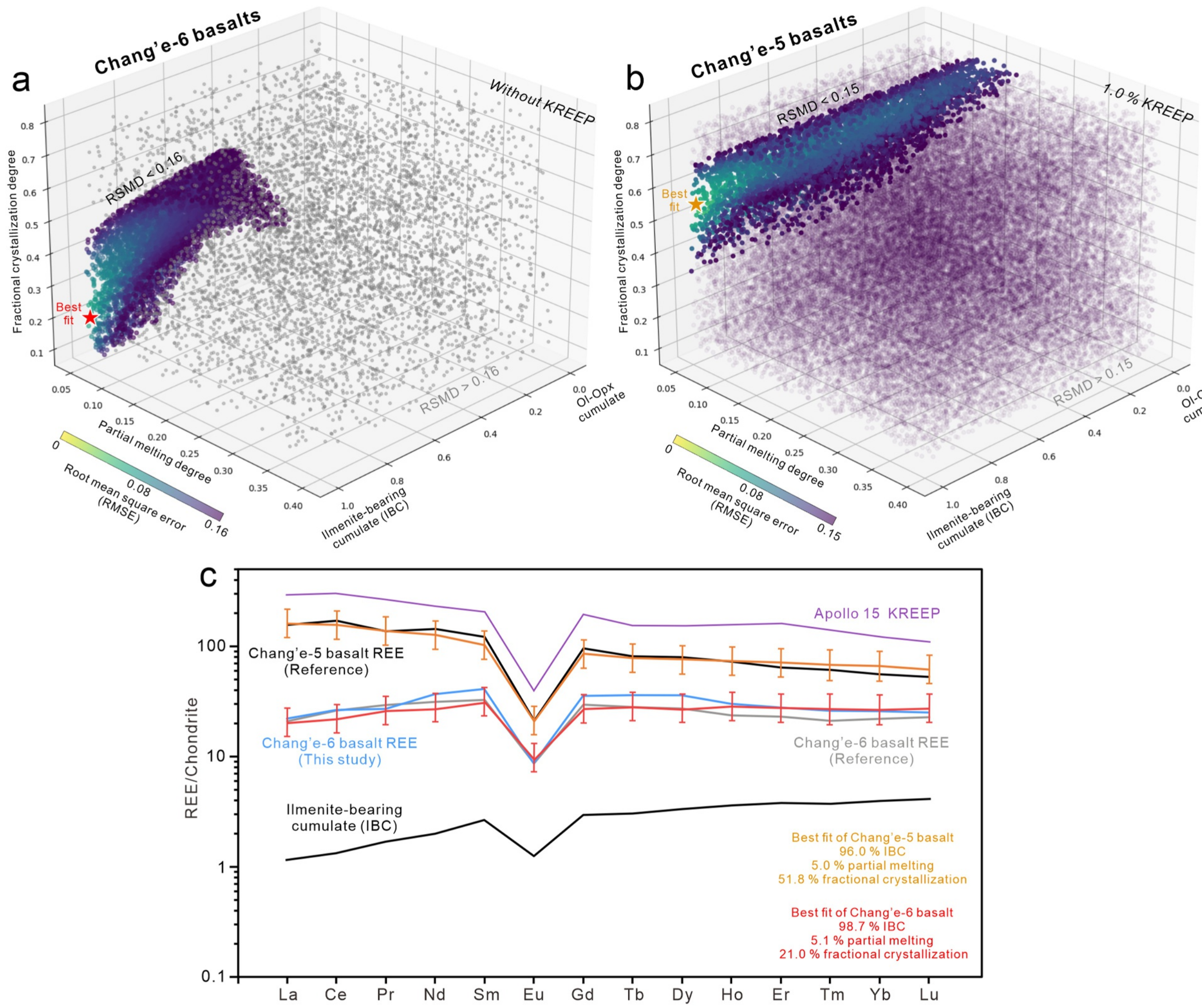

Figure 4. REE Monte Carlo modeling of Chang'e-6 and Chang'e-5 low-Ti basalts. (a) Three-dimensional REE Monte Carlo modeling results for Chang'e-6 basalts. (b) Three-dimensional REE Monte Carlo modeling results for Chang'e-5 basalts. (c) The comparison between measured REE in the Chang'e-6 (this study and Che et al., 2025) and Chang'e-5 basalts (Tian et al., 2021) and modeling results. The best fit for Chang'e-6 basalts is 98.7% IBC, 5.1% partial melting and 21% fractional crystallization. The best fit for Chang'e-5 basalts is 96.0% IBC, 5.0% partial melting and 51.8% fractional crystallization. The Apollo 15 KREEP data is from Clive Neal's Mare Basalt Database (https://www3.nd.edu/~cneal/Lunar-L/). The IBC REE data is collected from Hallis et al. (2014) and its references therein.

melting of late-stage ilmenite-bearing cumulates (C. Wang et al., 2024, 2025) formed at approximately 95–99 PCS (PCS-Per Cent Solid, Snyder et al., 1992), which can also match the observed results (Figure 3a).

Within the commonly adopted first-order petrogenetic framework for mare basalts, the range of possible primary melts for the Chang'e-6 and Chang'e-5 basalts can be discussed mainly in terms of three variables: (a) the mixing proportion between late-stage IBC and early-stage Ol-Opx cumulates, (b) the degree of partial melting, and (c) the degree of fractional crystallization (Hallis et al., 2014; Snyder et al., 1992). In this situation, a more precise distinction between these three processes would likely require more data for additional constraints, such as the REE (Figure 4). Based on the three factors mentioned above that may affect basalt composition, we introduced Monte Carlo modeling for Chang'e-6 REE (this study) and Chang'e-5 REE (Che et al., 2021) to evaluate the most likely mode of formation of these basalts (Section 2; Figure 4; Table S8). The degree of KREEP component participation is indicated by the results of radioactive isotopes in this study and previous studies (Zong et al., 2022; Z. Wang et al., 2024) (Figures 4a and 4b). The modeling results show that the modeled IBC end-member proportion in the Chang'e-6 mantle source must exceed 45%, and that a higher proportion could produce a better fit (Figure 4a). In fact, the best fit (RMSE = 0.04) was obtained from a 98.7% modeled IBC endmember proportion, and the observed REE patterns both in this study and previous study (Che et al., 2025) can be reproduced by 5.1% partial melting and 21.0% fractional crystallization (Figures 4a and 4c). In contrast, the modeling results of Chang'e-5 basalts show similar degree of partial melting and higher fractional crystallization degree than the Chang'e-6 basalts (Figures 4a and 4b). Specifically, the best fit (RMSE = 0.04) of Chang'e-5 mantle source is a 96.0% modeled IBC endmember proportion, and the observed REE pattern could be formed by 5.0% partial melting and 51.8% fractional crystallization (Figures 4b and 4c). These results indicate that the Chang'e-6 and Chang'e-5 basalts are both most likely to have originated from the shallow IBC and that they formed by a similar low degree of partial melting, but experienced different KREEP addition and fractional crystallization. Notably, differences in the degree of fractional crystallization can only affect the REE abundance of the final basalt, but cannot control the scale of partial melting in its source region. In this sense, fractional crystallization amplifies the observable REE divergence, while IBC heterogeneity remains the deeper petrogenetic control on source generation (See next section).

Based on the Chang'e-6 best-fitting fractional crystallization degree (~21.0%), we restored the composition of the Chang'e-6 primary melt and estimated its multiple saturation point (MSP) (Figure 3b). The MSP could be applied for constraining the P-T formation conditions of the Chang'e-6 melt because the primary magma was considered to be segregated from its mantle source under the MSP conditions (Elardo et al., 2015; Grove & Krawczynski, 2009; Longhi, 1992). The modeling result yields a MSP for the Chang'e-6 basalts at ~4.6 kbar and ~1198°C, where clinopyroxene and ilmenite are saturated (Figure 3b). This result indicates that there is more ilmenite and clinopyroxene in the Chang'e-6 mantle source compared to the Apollo low-Ti basalt source, dominated by olivine and clinopyroxene (Hallis et al., 2014; Neal & Taylor, 1992; Snyder et al., 1992), but is similar to the suggested shallow Chang'e-5 mantle source (~4 kbar and ~1170°C) (Haupt et al., 2023; C. Wang et al., 2024).

To provide an independent empirical check on the inferred P–T conditions of the Chang'e-6 basalts, clinopyroxene-liquid thermobarometers (Neave & Putirka, 2017; Putirka, 2008) were also calculated based on the early crystallized pyroxene compositions with high Mg# values (Mg# = 60–67). Thirty analysis points which passed Fe-Mg exchange equilibrium testing in the cpx-melt system were retained for calculation (Section 2; Figure S7 in Supporting Information S1) and the results showed that most high-Mg# clinopyroxenes crystallized at ~2–5 kbar and ~1120°C–1200°C (Figure 3b; Table S9), whose highest P-T conditions are close to the calculated MSP (Figure 3b). Therefore, we suggest that Chang'e-6 basalts are most likely to have originated from a shallow IBC source and the estimated depth is ~80–90 km, consistent with the prediction of the LMO hypothesis (Elkins-Tanton et al., 2011; Lin et al., 2017). Previous geodynamic studies indicated that the density difference between IBC and the underlying peridotite could result in a large-scale mantle overturn (Hess & Parmentier, 1995; Zhang et al., 2022). This process would introduce high-Ti components into deep early-stage cumulate, and their hybridization then partially melted to form the source region of high-Ti basalts (Haupt et al., 2024; Klaver et al., 2024; Mallik et al., 2019). However, recent studies argued that this overturn may be inefficient and was likely to have left partial IBC in the upper part of the lunar mantle (Xu et al., 2022; Zhao et al., 2019). This relatively shallow residual IBC could therefore be the mantle source of Chang'e-6 and Chang'e-5 basalts.

4.3. Asymmetric Ilmenite Abundances in the Nearside and Farside IBCs

Considering that both Chang'e-6 and Chang'e-5 young basalts originated from shallow IBCs, evaluating their source regions can enhance our understanding of the similarities and differences between IBCs on the nearside and farside. To place the inferred shallow source of the Chang'e-6 basalts into a broader context, we compiled major-element data for globally distributed young mare basalts (age <3.0 Ga) from remote-sensing data sets following Zhang et al. (2025) (Figure 5a; Table S10). These data can be divided into four groups, including the nearside mare units in the PKT, nearside mare units outside the PKT, farside mare units in the SPA basin and farside mare units outside the SPA basin (Figure 5a). The MSPs were calculated using the GeoPS program and can be applied to evaluating their P-T formation conditions (Section 2; Figure 5a; Table S10). The results show that most young magmas formed under pressures of 6–18 kbar, while a few basalts have shallow source regions, with pressures of 2–6 kbar (Figure 5a; Table S10).

To evaluate the properties of shallow IBCs, we extracted data with pressures less than 6 kbar (corresponding to a depth of approximately 120 km) and fitted it with the modeling results of IBC partial melting by pMelts program (Figures 5b and 5c and Table S11). Considering the variability of ilmenite abundance, we set the ilmenite abundance range to 0–33 wt% in the modeling, based on the IBC compositions in the previous study (Lin

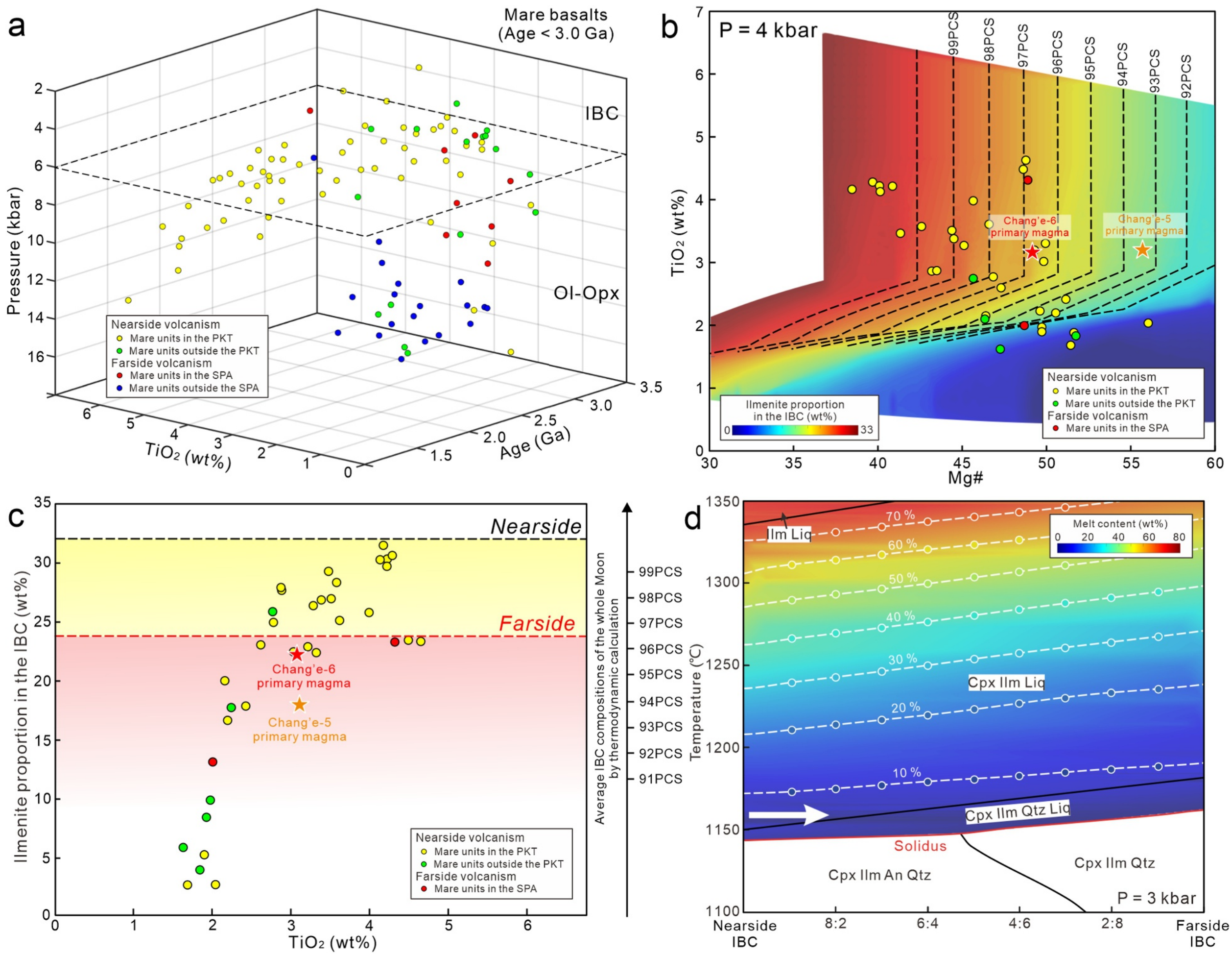

Figure 5. Thermodynamic calculation results for mare basalts from shallow IBC source. (a) The P-T condition estimation of the multiple saturation point of young lunar mare basalts based on the compositions from remote sensing observations. The extraction method of remote sensing data was from Zhang et al. (2025). (b) Melt composition formed by partial melting of IBCs with different ilmenite abundance from 0 to 33 wt% and their fitting results with basalts from a shallow source (<6 kbar). The pressure setting of 4 kbar corresponds to the average depth of IBC in the previous study (Lin et al., 2017). The 91PCS-99PCS represents the average level of the whole Moon based on the thermodynamic calculations (Lin et al., 2017). (c) The ilmenite proportion in the nearside and farside IBCs fitted from (b). (d) Phase diagram between upper limits of nearside IBC and farside IBC estimated in this study. The pressure setting of 3 kbar corresponds to the depth of the top of IBC in the previous study (Lin et al., 2017). The calculation results are shown in Table S12.

et al., 2017) (Section 2). Given the compositional variability of ilmenite and the limitations of the available remote sensing whole-rock data, this parameter is interpreted here as an effective or apparent modal ilmenite proportion in the modeled source, rather than as an exact mineralogical abundance. The modeling and matching results show that these young basalts could have originated from the shallow IBC with various ilmenite abundance (Figures 5b and 5c). Specifically, the mare units in the PKT generally have mantle sources containing ∼16–32 wt% ilmenite, except for a few data points (Figures 5b and 5c). This estimation is consistent with ilmenite abundance in the nearside IBC (average ∼28.8 wt%) revealed by Chang'e-5 high-Ti glass beads (Z. Li et al., 2026). And, the upper limit of their ilmenite abundance has exceeded the level in LMO modeling calculations (91PCS to 99PCS) conducted under a global magma ocean condition (Lin et al., 2017) (Figures 5b and 5c), as suggested by Z. Li et al. (2026). In this case, these results may suggest an IBC with higher ilmenite abundance on the nearside than the global average level without considering regional heterogeneity. In addition, our results indicate that the source of Chang'e-5 basalts contains ∼18 wt% ilmenite, which is consistent with previous estimation (∼15–25 wt% ilmenite) based on the high field strength elements (C. Wang et al., 2024). In contrast, those mantle sources of mare units outside the PKT, both nearside and farside, typically have relatively lower ilmenite abundance (Figures 5b and 5c). Importantly, the farside mare units in the SPA basin only have ∼13–24 wt% ilmenite in the IBC and the Chang'e-6 mantle source has approached their upper limit (Figures 5b and 5c). These comparisons indicate that the ilmenite abundance in the IBCs on the two lunar hemispheres is asymmetric and the nearside upper limit is ∼8 wt% higher than farside (Figures 5b and 5c). However, the nearside and farside ranges overlap substantially, and the nearside data set is much denser than the farside data set. Therefore, the Chang'e-6 basalts may not be interpreted as representative of the entire farside hemisphere. Instead, we describe this pattern only as an apparent difference in the upper limit of the currently available data set, with the nearside extending to higher apparent ilmenite-rich shallow-source compositions than the farside. This apparent asymmetry in the existing data framework may reflect a real hemispheric contrast, but it may also partly result from incomplete farside sampling and could be modified by future sample returns.

4.4. IBCs With Various Ilmenite Abundance Triggered Asymmetric Lunar Volcanism

To evaluate the influence of IBC asymmetry on magma production, we conducted phase equilibrium calculations based on the upper limits of nearside IBC and farside IBC compositions determined in this study (Figure 5d; Table S12). The calculated phase relations show that the nearside IBC composition has a lower solidus temperature than the farside IBC composition, by approximately ∼20°C–30°C (Figure 5d; Table S12). This difference could be attributed solely to the higher modal abundance of ilmenite or reflects the overall Fe-Ti-rich and relatively fertile character of the nearside IBC source, which is expected to make the mantle assemblage more fertile and more susceptible to partial melting. This result indicates that the nearside IBC with higher ilmenite abundance tends to produce more melt than farside IBC under the same temperature of partial melting (Figure 5d). In this scenario, the heterogeneity of the IBCs may have a significant influence on the partial melting process and the formation of magma source regions.

The origin of the observed lunar mare basalt asymmetry on the nearside and farside is a long-standing issue in lunar science (Kring & Durda, 2012). A series of remote sensing data suggested similar age distributions (Haruyama et al., 2009; Head et al., 2023; Qian et al., 2024; X. Wang et al., 2024) of nearside and farside volcanism, but a 20 times volume difference between these two hemispheres (Taguchi et al., 2017). This asymmetry was considered to be attributed to the thinner crust on the nearside than that on the farside (Head et al., 2024; Head & Wilson, 1992; Solomon, 1975). However, the basalt volume does not significantly increase even in some farside regions with similar or thinner crustal thickness than that on the nearside (e.g., Mare Moscoviense and SPA basin) (Charlier et al., 2018; Head & Wilson, 2017; Head et al., 2024; Taguchi et al., 2017) (Figure S8 in Supporting Information S1), indicating that crustal thickness is not the only factor controlling the distribution of mare basalt. In contrast, the mechanism of radioactive heating (Borg et al., 2004; Warren, 1985) or melting point decrease (Elardo et al., 2020) caused by deep heterogeneous KREEP is also difficult to envision as playing a role in young magmatism difference between nearside and farside. Specifically, young Chang'e-5 and Chang'e-6 basalts both exhibit relatively depleted Sr-Nd isotope characteristics (Cui et al., 2024; Tian et al., 2021; Zhou et al., 2025), indicating the rare contribution of a KREEP reservoir (<1%). Although a study suggested that KREEP heating is indirect and does not directly participate in the Chang'e-5 source region (Elardo et al., 2025), this mechanism may be localized and difficult to lead to the volume increase of the nearside basalt outside of the PKT (Taguchi et al., 2017).

Alternatively, the mare basalt asymmetry dominated by IBC heterogeneity is possible but the specific mechanism still needs further clarification (Su et al., 2022; C. Wang et al., 2024, 2025). Our study suggests that the nearside IBC beneath the PKT contains ilmenite abundances significantly higher than that beneath the farside SPA basin, which possibly leads to a decrease of melting point and an increase in the degree of partial melting (Figure 6). In addition, ilmenite crystallization and accumulation are closely associated with Fe–Ti enrichment during late-stage lunar magma ocean differentiation, a higher ilmenite abundance also implies a more Fe-rich, Ti-rich, and compositionally enriched mantle source beneath the nearside. Such bulk compositional enrichment may influence mare basalt generation through several coupled effects. First, a Fe–Ti-rich IBC source is expected to have a lower solidus and higher melt productivity than a relatively Mg-rich farside source, thereby increasing the degree of partial melting under comparable thermal conditions (Figure 6). Second, the higher density of Fe–Ti-rich cumulates may promote more vigorous gravitational instability and mantle overturn, potentially enhancing the redistribution of fertile materials into melting regions (Tokle et al., 2021). Third, an enriched nearside mantle source may have retained more incompatible elements and heat-producing components during late-stage lunar magma ocean evolution, thereby modifying the local thermal state and long-term melt productivity. Importantly, the estimated higher mantle potential temperature from sample compositions on the nearside than farside (He et al., 2025) could further expand the disparity in the scale volcanism on the two hemispheres.

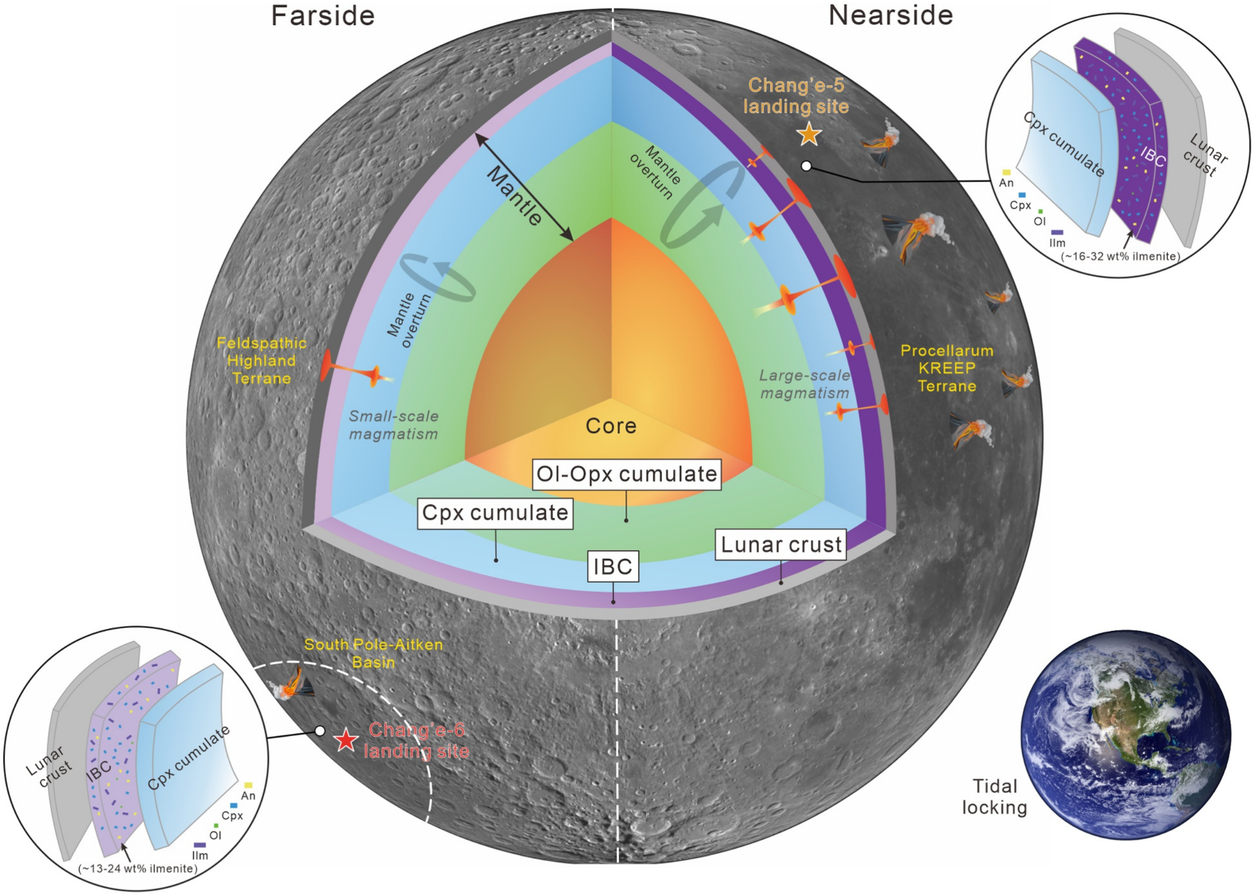

Figure 6. Schematic diagrams of the mechanism of lunar mare basalt asymmetry (Modified from Z. Li et al. (2026)). The lunar nearside and farside have different magmatism. The magmatism on the lunar nearside is significantly larger in scale than that on the farside, while the mare units on the far side are mainly concentrated in the SPA basin. The diagram shows that the IBC beneath the nearside (mainly in the PKT) may contain ilmenite abundances significantly higher than the farside, leading to an increase in the degree of partial melting and large-scale magmatism. The darker and lighter purple colors of the IBC layer indicate higher and lower ilmenite abundances on the nearside and farside, respectively. The detailed layer structure was modified based on the Ju et al. (2022) and this schematic diagram is not drawn to actual scale. Ol-olivine; Opx-orthopyroxene; Cpx-clinopyroxene; An-anorthite; Ilm-ilmenite.

Similarly, this IBC heterogeneity hypothesis was also supported by the lunar global TiO_2 distribution observed by remote sensing (Sato et al., 2017), that is, most of the high-Ti basalts that require IBC to participate in the source region formation are concentrated in or near the PKT while lacking on the farside. In addition, a series of data indicate lateral density variations within the lunar crust and upper mantle at a global scale, especially the higher density, Bouguer gravity anomaly, gravity gradient and high electrical conductivity beneath the nearside PKT (Besserer et al., 2014; Grimm, 2013). These observations suggest a possible enrichment in Fe-bearing materials with high density beneath the PKT, which is consistent with the existence of a predicted ilmenite-rich layer.

Therefore, the nearside–farside IBC contrast likely records not only different ilmenite abundances, but also broader hemispheric differences in mantle fertility, Fe–Ti enrichment, density structure, and late-stage lunar magma ocean differentiation. This phenomenon could be attributed to either inherited asymmetry in the LMO crystallization (Ohtake et al., 2012) or dynamic redistribution of compositionally stratified layers by thermo-mechanical forcing during the SPA basin-forming impact event (Jones et al., 2022; Zhang et al., 2022). Overall, our findings establish that the nearside-farside heterogeneous IBC with various ilmenite abundance have different effects and could cause distinctive volcanic evolution and differential mare basalt distribution in each hemisphere.

5. Conclusions

China's Chang'e-6 mission returned the first samples from the lunar farside, collected within the South Pole-Aitken basin. In this study, we characterized the petrology and geochemistry of the Chang'e-6 basalts and integrated major-element petrological modeling, Monte Carlo trace-element modeling, and thermodynamic calculations to constrain their mantle source. These independent approaches consistently indicate that both Chang'e-6 and Chang'e-5 basalts were generated by partial melting of shallow, ilmenite-bearing cumulate reservoirs derived from late-stage lunar magma ocean crystallization.

Combined remote-sensing observations and thermodynamic calculations suggest that the ilmenite-bearing cumulates beneath the farside South Pole-Aitken basin generally contained less ilmenite than those beneath the nearside Procellarum KREEP Terrane. Although the inferred ranges overlap and substantial regional heterogeneity likely existed within both hemispheres, the higher upper limit of ilmenite abundance on the nearside indicates a pronounced hemispheric asymmetry in the distribution of late-stage lunar magma ocean cumulates. Because ilmenite-rich cumulates have lower solidus temperatures and can generate Ti-rich melts at relatively low degrees of partial melting, their greater abundance beneath the nearside may have enhanced mantle fusibility and promoted more extensive and longer-lived mare volcanism. Conversely, the lower ilmenite abundance inferred for the farside mantle may have limited melt production, contributing to the restricted distribution and smaller volume of farside mare basalts. These results link the compositional heterogeneity inherited from lunar magma ocean crystallization and subsequent mantle reorganization to the hemispheric asymmetry of lunar volcanism.

Conflict of Interest

The authors declare no conflicts of interest relevant to this study.

Availability Statement

The Supporting Information S1 in this study could be found at Z. Li et al. (2026) and is available at figshare repository at https://doi.org/10.6084/m9.figshare.31023856.v1 (Z. Li, 2026). The PETROLOG program for fractional crystallization is available at Danyushevsky and Plechov (2011). The GeoPS program is available at Xiang and Connolly (2022) and the pMelts program is available at Ghiorso et al. (2002).

Acknowledgments
We are grateful to the China National Space Administration (CNSA) for providing the Chang'e-6 samples. This study was supported by the National Natural Science Foundation of China (42241107). Y. Q. was funded by the HK RGC GRF 17307025 and JLFS/P-702/24.

References

Astudillo Manosalva, D. F., & Elardo, S. M. (2024). Assessing the accuracy of phase equilibrium software in reproducing the liquidus multiple saturation conditions of lunar and Martian basalt compositions. *Meteorit Planet Sci*, *59*(2), 260–285. https://doi.org/10.1111/maps.14117

Besserer, J., Nimmo, F., Wieczorek, M. A., Weber, R. C., Kiefer, W. S., McGovern, P. J., et al. (2014). GRAIL gravity constraints on the vertical and lateral density structure of the lunar crust. *Geophysical Research Letters*, *41*(16), 5771–5777. https://doi.org/10.1002/2014GL060240

Borg, L. E., Shearer, C. K., Asmerom, Y., & Papike, J. J. (2004). Prolonged KREEP magmatism on the moon indicated by the youngest dated lunar igneous rock. *Nature*, *432*(7014), 209–211. https://doi.org/10.1038/nature03070

Charlier, B., Grove, T. L., Namur, O., & Holtz, F. (2018). Crystallization of the lunar magma ocean and the primordial mantle-crust differentiation of the moon. *Geochimica et Cosmochimica Acta*, *234*, 50–69. https://doi.org/10.1016/j.gca.2018.05.006

Che, X., Long, T., Nemchin, A., Xie, S., Qiao, L., Li, Z., et al. (2025). Isotopic and compositional constraints on the source of basalt collected from the lunar far side. *Science*, *387*(6740), 1306–1310. https://doi.org/10.1126/science.adt3332

Che, X., Nemchin, A., Liu, D., Long, T., Wang, C., Norman, M. D., et al. (2021). Age and composition of young basalts on the moon, measured from samples returned by Chang'e-5. *Science*, *374*(6569), 887–890. https://doi.org/10.1126/science.abl7957

Cone, K. A. (2021). ApolloBasalt DB_V2, version 1.0 (interdisciplinary Earth data alliance).

Cui, Z., Yang, Q., Zhang, Y. Q., Wang, C., Xian, H., Chen, Z., et al. (2024). A sample of the Moon's far side retrieved by Chang'e-6 contains 2.83-billion-year-old basalt. *Science*, *386*(6728), 1395–1399. https://doi.org/10.1126/science.adt1093

Danyushevsky, L. V. (2001). The effect of small amounts of H2O on crystallisation of mid-ocean ridge and backarc basin magmas. *Journal of Volcanology and Geothermal Research*, *110*(3), 265–280. https://doi.org/10.1016/S0377-0273(01)00213-X

Danyushevsky, L. V., & Plechov, P. (2011). Petrolog3: Integrated software for modeling crystallization processes. *Geochemistry, Geophysics, Geosystems*, *12*(7). https://doi.org/10.1029/2011GC003516

Elardo, S. M., & Astudillo Manosalva, D. F. (2023). Complexity and ambiguity in the relationships between major lunar crustal lithologies and meteoritic clasts inferred from major and trace element modeling. *Geochimica et Cosmochimica Acta*, *354*, 13–26. https://doi.org/10.1016/j.gca.2023.05.020

Elardo, S. M., Cone, K. A., Siegler, M. A., Williams, S. J., & Palin, R. M. (2025). A shallow mantle source for the Chang'e-5 lavas reveals how top-down heating prolonged lunar magmatism. *Science Advances*, *11*(29), eadr1486. https://doi.org/10.1126/sciadv.adr1486

Elardo, S. M., Laneuville, M., McCubbin, F. M., & Shearer, C. K. (2020). Early crust building enhanced on the Moon's nearside by mantle melting-point depression. *Nature Geoscience*, *13*(5), 339–343. https://doi.org/10.1038/s41561-020-0559-4

Elardo, S. M., Shearer, C. K., Jr., Fagan, A. L., Borg, L. E., Gaffney, A. M., Burger, P. V., et al. (2014). The origin of young mare basalts inferred from lunar meteorites Northwest Africa 4734, 032, and LaPaz icefield 02205. *Meteoritics & Planetary Science*, *49*(2), 261–291. https://doi.org/10.1111/maps.12239

Elardo, S. M., Shearer, C. K., Vander Kaaden, K. E., McCubbin, F. M., & Bell, A. S. (2015). Petrogenesis of primitive and evolved basalts in a cooling moon: Experimental constraints from the youngest known lunar magmas. *Earth and Planetary Science Letters*, *422*, 126–137. https://doi.org/10.1016/j.epsl.2015.04.014

Elkins-Tanton, L. T., Burgess, S., & Yin, Q.-Z. (2011). The lunar magma ocean: Reconciling the solidification process with lunar petrology and geochronology. *Earth and Planetary Science Letters*, *304*(3), 326–336. https://doi.org/10.1016/j.epsl.2011.02.004

Ford, C. E., Russell, D. G., Craven, J. A., & Fisk, M. R. (1983). Olivine-liquid equilibria: Temperature, pressure and composition dependence of the crystal/liquid cation partition coefficients for Mg, Fe2+, Ca and Mn. *Journal of Petrology*, *24*(3), 256–266. https://doi.org/10.1093/petrology/24.3.256

Ghiorso, M. S., Hirschmann, M. M., Reiners, P. W., & Kress III, V. C. (2002). The pMELTS: A revision of MELTS for improved calculation of phase relations and major element partitioning related to partial melting of the mantle to 3 GPa. *Geochemistry, Geophysics, Geosystems*, *3*(5), 1–35. https://doi.org/10.1029/2001GC000217

Grimm, R. (2013). Geophysical constraints on the lunar Procellarum KREEP Terrane. *Journal of Geophysical Research (Planets)*, *118*(4), 768–778. https://doi.org/10.1029/2012JE004114

Grove, T. L., & Krawczynski, M. J. (2009). Lunar mare volcanism: Where did the magmas come from? *Elements*, *5*(1), 29–34. https://doi.org/10.2113/gselements.5.1.29

Hallis, L. J., Anand, M., & Strekopytov, S. (2014). Trace-element modelling of mare basalt parental melts: Implications for a heterogeneous lunar mantle. *Geochimica et Cosmochimica Acta*, *134*, 289–316. https://doi.org/10.1016/j.gca.2014.01.012

Haruyama, J., Ohtake, M., Matsunaga, T., Morota, T., Honda, C., Yokota, Y., et al. (2009). Long-lived volcanism on the lunar farside revealed by SELENE terrain camera. *Science*, *323*(5916), 905–908. https://doi.org/10.1126/science.1163382

Haupt, C. P., Renggli, C. J., Klaver, M., Steenstra, E. S., Berndt, J., Rohrbach, A., & Klemme, S. (2023). Experimental and petrological investigations into the origin of the lunar Chang'e-5 basalts. *Icarus*, *402*, 115625. https://doi.org/10.1016/j.icarus.2023.115625

Haupt, C. P., Renggli, C. J., Rohrbach, A., Berndt, J., Schwinger, S., Maurice, M., et al. (2024). Trace element partitioning in the lunar magma ocean: An experimental study. *Contributions to Mineralogy and Petrology*, *179*(5), 45. https://doi.org/10.1007/s00410-024-02118-z

He, S., Li, Y., Zhu, X., Chen, J., Li, Z., Li, T., et al. (2025). A relatively cool lunar farside mantle inferred from Chang'e-6 basalts and remote sensing. *Nature Geoscience*, *18*(11), 1103–1108. https://doi.org/10.1038/s41561-025-01815-z

Head, J. W., Wang, X., Lark, L. H., Wilson, L., & Qian, Y. (2024). Lunar nearside-farside mare basalt asymmetry: The combined role of global crustal thickness variations and south pole-aitken (SPA) basin-induced lithospheric thickening. *Geophysical Research Letters*, *51*(22), e2024GL110510. https://doi.org/10.1029/2024GL110510

Head, J. W., & Wilson, L. (1992). Lunar mare volcanism: Stratigraphy, eruption conditions, and the evolution of secondary crusts. *Geochimica et Cosmochimica Acta*, *56*(6), 2155–2175. https://doi.org/10.1016/0016-7037(92)90183-J

Head, J. W., & Wilson, L. (2017). Generation, ascent and eruption of magma on the moon: New insights into source depths, magma supply, intrusions and effusive/explosive eruptions (Part 2: Predicted emplacement processes and observations). *Icarus*, *283*, 176–223. https://doi.org/10.1016/j.icarus.2016.05.031

Head, J. W., Wilson, L., Hiesinger, H., van der Bogert, C., Chen, Y., Dickson, J. L., et al. (2023). Lunar mare basaltic volcanism: Volcanic features and emplacement processes. *Reviews in Mineralogy and Geochemistry*, *89*(1), 453–507. https://doi.org/10.2138/rmg.2023.89.11

Hess, P. C., & Parmentier, E. M. (1995). A model for the thermal and chemical evolution of the Moon's interior: Implications for the onset of mare volcanism. *Earth and Planetary Science Letters*, *134*(3), 501–514. https://doi.org/10.1016/0012-821X(95)00138-3

Hiesinger, H., van der Bogert, C., Michael, G., Schmedemann, N., Iqbal, W., Robbins, S., et al. (2023). The lunar cratering chronology. *Reviews in Mineralogy and Geochemistry*, *89*(1), 401–451. https://doi.org/10.2138/rmg.2023.89.10

Holland, T. J. B., Green, E. C. R., & Powell, R. (2018). Melting of peridotites through to granites: A simple thermodynamic model in the system KNCFMASHTOCr. *Journal of Petrology*, *59*(5), 881–900. https://doi.org/10.1093/petrology/egy048

Johnson, T. E., Morrissey, L. J., Nemchin, A. A., Gardiner, N. J., & Snape, J. F. (2021). The phases of the moon: Modelling crystallisation of the lunar magma ocean through equilibrium thermodynamics. *Earth and Planetary Science Letters*, *556*, 116721. https://doi.org/10.1016/j.epsl.2020.116721

Jones, M. J., Evans, A. J., Johnson, B. C., Weller, M. B., Andrews-Hanna, J. C., Tikoo, S. M., & Keane, J. T. (2022). A South Pole–Aitken impact origin of the lunar compositional asymmetry. *Science Advances*, *8*(14), eabm8475. https://doi.org/10.1126/sciadv.abm8475

Ju, D. Y., Pang, R. L., Li, R., & Du, W. (2022). The initial lunar mantle structure constrained by thermodynamic simulation. *Acta Petrologica Sinica*, *38*, 1025–1042.

Kato, S., Morota, T., Yamaguchi, Y., Watanabe, S.-i., Otake, H., & Ohtake, M. (2017). Magma source transition of lunar mare volcanism at 2.3 Ga. *Meteoritics & Planetary Science*, *52*(9), 1899–1915. https://doi.org/10.1111/maps.12896

Klaver, M., Klemme, S., Liu, X.-N., Hin, R. C., Coath, C. D., Anand, M., et al. (2024). Titanium-rich basaltic melts on the Moon modulated by reactive flow processes. *Nature Geoscience*, *17*(2), 118–123. https://doi.org/10.1038/s41561-023-01362-5

Kring, D. A., & Durda, D. D. (2012). A global lunar landing site study to provide the scientific context for exploration of the moon. https://doi.org/10.1002/2013JE004530

Laneuville, M., Taylor, J., & Wieczorek, M. A. (2018). Distribution of radioactive heat sources and thermal history of the moon. *Journal of Geophysical Research: Planets*, *123*(12), 3144–3166. https://doi.org/10.1029/2018JE005742

Lawrence, D. J., Feldman, W. C., Barraclough, B. L., Binder, A. B., Elphic, R. C., Maurice, S., et al. (2000). Thorium abundances on the lunar surface. *Journal of Geophysical Research*, *105*(E8), 20307–20331. https://doi.org/10.1029/1999JE001177

Li, Q.-L., Zhou, Q., Liu, Y., Xiao, Z., Lin, Y., Li, J. H., et al. (2021). Two-billion-year-old volcanism on the moon from Chang'e-5 basalts. *Nature*, *600*(7887), 54–58. https://doi.org/10.1038/s41586-021-04100-2

Li, Z. (2026). Figshare. https://doi.org/10.6084/m9.figshare.31023856.v1

Li, Z., Zhang, B., Qian, Y., Head, J. W., Long, T., & Che, X. (2026). Elevated ilmenite in lunar nearside cumulates revealed by extremely high-Ti glass beads augmented large-scale volcanism. *Communications Earth & Environment*, *7*(1), 272. https://doi.org/10.1038/s43247-026-03300-w

Lin, Y., Tronche, E. J., Steenstra, E. S., & van Westrenen, W. (2017). Experimental constraints on the solidification of a nominally dry lunar magma ocean. *Earth and Planetary Science Letters*, *471*, 104–116. https://doi.org/10.1016/j.epsl.2017.04.045

Longhi, J. (1992). Experimental petrology and petrogenesis of mare volcanics. *Geochimica et Cosmochimica Acta*, *56*(6), 2235–2251. https://doi.org/10.1016/0016-7037(92)90186-M

Luo, B., Wang, Z., Song, J., Qian, Y., He, Q., Li, Y., et al. (2023). The magmatic architecture and evolution of the Chang'e-5 lunar basalts. *Nature Geoscience*, *16*(4), 301–308. https://doi.org/10.1038/s41561-023-01146-x

Mallik, A., Ejaz, T., Shcheka, S., & Garapic, G. (2019). A petrologic study on the effect of mantle overturn: Implications for evolution of the lunar interior. *Geochimica et Cosmochimica Acta*, *250*, 238–250. https://doi.org/10.1016/j.gca.2019.02.014

McDonough, W. F., & Sun, S. S. (1995). The composition of the Earth. *Chemical Geology*, *120*, 223–253.

McKay, G., Le, L., & Wagstaff, J. (1991). Constraints on the origin of the mare basalt europium anomaly: REE partition coefficients for pigeonite. In *Lunar and planetary science conference*.883.

McKay, G. A. (1986). Crystal/liquid partitioning of REE in basaltic systems: Extreme fractionation of REE in olivine. *Geochimica et Cosmochimica Acta*, *50*(1), 69–79. https://doi.org/10.1016/0016-7037(86)90049-9

Meyer, C., Jr., Brett, R., Hubbard, N. J., Morrison, D. A., McKay, D. S., Aitken, F. K., et al. (1971). Mineralogy, chemistry, and origin of the KREEP component in soil samples from the ocean of storms. *Lunar and Planetary Science Conference Proceedings*, *2*, 393.

Nakamura, Y., Fujimaki, H., Nakamura, N., Tatsumoto, M., McKay, G. A., & Wagstaff, J. (1986). Hf, Zr, and REE partition coefficients between ilmenite and liquid: Implications for lunar petrogenesis. *Journal of Geophysical Research*, *91*(B4), 239–250. https://doi.org/10.1029/JB091iB04p0D239

Neal, C. R., & Taylor, L. A. (1992). Petrogenesis of mare basalts: A record of lunar volcanism. *Geochimica et Cosmochimica Acta*, *56*(6), 2177–2211. https://doi.org/10.1016/0016-7037(92)90184-K

Neave, D. A., & Putirka, K. D. (2017). A new clinopyroxene-liquid barometer, and implications for magma storage pressures under Icelandic rift zones. *American Mineralogist*, *102*(4), 777–794. https://doi.org/10.2138/am-2017-5968

Nelson, D. M., Koeber, S. D., Daud, K., Robinson, M. S., Watters, T. R., Banks, M. E., & Williams, N. R. (2014). Mapping lunar maria extents and lobate scarps using LROC image products.

Nielsen, R. L. (1985). EQUIL: A program for the modeling of low-pressure differentiation processes in natural mafic magma bodies. *Computers & Geosciences*, *11*(5), 531–546. https://doi.org/10.1016/0098-3004(85)90084-6

Nyquist, L. E. (1977). Lunar Rb-Sr chronology. *Physics and Chemistry of the Earth*, *10*, 103–142.

Nyquist, L. E., Hubbard, N. J., Gast, P. W., Bansal, B. M., Weismann, H., & Jahn, B. (1973). Rb-Sr systematics for chemically defined Apollo 15 and 16 materials. *Lunar and Planetary Science Conference Proceedings*, *4*, 1823.

Ohtake, M., Takeda, H., Matsunaga, T., Yokota, Y., Haruyama, J., Morota, T., et al. (2012). Asymmetric crustal growth on the Moon indicated by primitive farside highland materials. *Nature Geoscience*, *5*(6), 384–388. https://doi.org/10.1038/ngeo1458

Papike, J. J., Hodges, F. N., Bence, A. E., Cameron, M., & Rhodes, J. M. (1976). Mare basalts: Crystal chemistry, mineralogy, and petrology. *Reviews of Geophysics*, *14*(4), 475–540. https://doi.org/10.1029/RG014i004p00475

Pasckert, J. H., Hiesinger, H., & van der Bogert, C. H. (2018). Lunar farside volcanism in and around the South Pole–Aitken basin. *Icarus*, *299*, 538–562. https://doi.org/10.1016/j.icarus.2017.07.023

Phinney, W. C., & Morrison, D. A. (1990). Partition coefficients for calcic plagioclase: Implications for Archean anorthosites. *Geochimica et Cosmochimica Acta*, *54*(6), 1639–1654. https://doi.org/10.1016/0016-7037(90)90397-4

Putirka, K. D. (2008). Thermometers and barometers for volcanic systems. *Reviews in Mineralogy and Geochemistry*, *69*(1), 61–120. https://doi.org/10.2138/rmg.2008.69.3

Qian, Y., Head, J., Michalski, J., Wang, X., van der Bogert, C. H., Hiesinger, H., et al. (2024). Long-lasting farside volcanism in the Apollo basin: Chang'e-6 landing site. *Earth and Planetary Science Letters*, *637*, 118737. https://doi.org/10.1016/j.epsl.2024.118737

Robinson, K. L., Treiman, A. H., & Joy, K. H. (2012). Basaltic fragments in lunar feldspathic meteorites: Connecting sample analyses to orbital remote sensing. *Meteoritics & Planetary Science*, *47*(3), 387–399. https://doi.org/10.1111/j.1945-5100.2012.01344.x

Sato, H., Robinson, M. S., Lawrence, S. J., Denevi, B. W., Hapke, B., Jolliff, B. L., & Hiesinger, H. (2017). Lunar mare TiO2 abundances estimated from UV/Vis reflectance. *Icarus*, *296*, 216–238. https://doi.org/10.1016/j.icarus.2017.06.013

Smith, D. E., Zuber, M. T., Neumann, G. A., Lemoine, F. G., Mazarico, E., Torrence, M. H., et al. (2010). Initial observations from the Lunar Orbiter Laser Altimeter (LOLA). *Geophysical Research Letters*, *37*(18). https://doi.org/10.1029/2010GL043751

Snyder, G. A., Taylor, L. A., & Neal, C. R. (1992). A chemical model for generating the sources of mare basalts: Combined equilibrium and fractional crystallization of the lunar magmasphere. *Geochimica et Cosmochimica Acta*, *56*(10), 3809–3823. https://doi.org/10.1016/0016-7037(92)90172-F

Solomon, S. C. (1975). Mare volcanism and lunar crustal structure. *Lunar and Planetary Science Conference Proceedings*, *1*, 1021–1042.

Su, B., Yuan, J., Chen, Y., Yang, W., Mitchell, R. N., Hui, H., et al. (2022). Fusible mantle cumulates trigger young mare volcanism on the cooling moon. *Science Advances*, *8*(42), eabn2103. https://doi.org/10.1126/sciadv.abn2103

Taguchi, M., Morota, T., & Kato, S. (2017). Lateral heterogeneity of lunar volcanic activity according to volumes of mare basalts in the farside basins. *Journal of Geophysical Research: Planets*, *122*(7), 1505–1521. https://doi.org/10.1002/2016JE005246

Tian, H.-C., Wang, H., Chen, Y., Yang, W., Zhou, Q., Zhang, C., et al. (2021). Non-KREEP origin for Chang'e-5 basalts in the procellarum KREEP terrane. *Nature*, *600*(7887), 59–63. https://doi.org/10.1038/s41586-021-04119-5

Tokle, L., Hirth, G., Liang, Y., Raterron, P., & Dygert, N. (2021). The effect of pressure and Mg-Content on ilmenite rheology: Implications for lunar cumulate mantle overturn. *Journal of Geophysical Research: Planets*, *126*(1), e2020JE006494. https://doi.org/10.1029/2020JE006494

Tomlinson, E. L., & Holland, T. J. B. (2021). A thermodynamic model for the subsolidus evolution and melting of peridotite. *Journal of Petrology*, *62*(1), egab012. https://doi.org/10.1093/petrology/egab012

Wang, C., Qian, Y., Wang, J., Liu, L., Zhang, L., Chen, Z., et al. (2025). The source and thermal driver of young (<3.0 Ga) lunar volcanism. *Science Advances*, *11*, eadv9085. https://doi.org/10.1126/sciadv.adv9085

Wang, C., Xu, Y.-G., Zhang, L., Chen, Z., Xia, X., Lin, M., & Guo, F. (2024). A shallow (<100 km) ilmenite-bearing pyroxenitic source for young lunar volcanism. *Earth and Planetary Science Letters*, *639*, 118770. https://doi.org/10.1016/j.epsl.2024.118770

Wang, X., Head, J. W., Chen, Y., Zhao, F., Kreslavsky, M. A., Wilson, L., et al. (2024). Lunar farside south pole-aitken basin interior: Evidence for more extensive central cryptomaria in the south pole-aitken compositional anomaly (SPACA). *Journal of Geophysical Research: Planets*, *129*(5), e2023JE008176. https://doi.org/10.1029/2023JE008176

Wang, Z., Zong, K., Li, Y., Li, J., He, Q., Zou, Z., et al. (2024). Young KREEP-like mare volcanism from Oceanus Procellarum. *Geochimica et Cosmochimica Acta*, *373*, 17–34. https://doi.org/10.1016/j.gca.2024.03.029

Warren, P. H. (1985). The magma ocean concept and lunar evolution. *Annual Review of Earth and Planetary Sciences*, *13*(1), 201–240. https://doi.org/10.1146/annurev.ea.13.050185.001221

Wieczorek, M. A., Neumann, G. A., Nimmo, F., Kiefer, W. S., Taylor, G. J., Melosh, H. J., et al. (2013). The crust of the Moon as seen by GRAIL. *Science*, *339*(6120), 671–675. https://doi.org/10.1126/science.1231530

Xiang, H., & Connolly, J. A. D. (2022). GeoPS: An interactive visual computing tool for thermodynamic modelling of phase equilibria. *Journal of Metamorphic Geology*, *40*(2), 243–255. https://doi.org/10.1111/jmg.12626

Xu, M., Jing, Z., Van Orman, J. A., Yu, T., & Wang, Y. (2022). Experimental evidence supporting an overturned iron-titanium-rich melt layer in the deep lunar interior. *Geophysical Research Letters*, *49*(13), e2022GL099066. https://doi.org/10.1029/2022GL099066

Yao, L., Sun, C., & Liang, Y. (2012). A parameterized model for REE distribution between low-Ca pyroxene and basaltic melts with applications to REE partitioning in low-Ca pyroxene along a mantle adiabat and during pyroxenite-derived melt and peridotite interaction. *Contributions to Mineralogy and Petrology*, *164*(2), 261–280. https://doi.org/10.1007/s00410-012-0737-5

Yin, C., Chen, J., Fu, X., Cao, H., Lu, X., Liu, Y., et al. (2025). Petrogenesis of Chang'e-6 basalts and implication for the young volcanism on the lunar farside. *The Astrophysical Journal Letters*, *981*(1), L2. https://doi.org/10.3847/2041-8213/adaf20

Yuan, J. Y., Chen, D., Zhang, X., Li, C., Tian, W., Yang, W., & Su, W. (2022). Quantitative analysis of bulk composition of small-size lunar samples using energy dispersive X-ray spectroscopy. *Atomic Spectroscopy*, *43*(4), 292–302. https://doi.org/10.46770/AS.2022.003

Zhang, N., Ding, M., Zhu, M.-H., Li, H., Li, H., & Yue, Z. (2022). Lunar compositional asymmetry explained by mantle overturn following the South Pole–Aitken impact. *Nature Geoscience*, *15*(1), 37–41. https://doi.org/10.1038/s41561-021-00872-4

Zhang, Q. W. L., Yang, M. H., Li, Q. L., Liu, Y., Yue, Z. Y., Zhou, Q., et al. (2024). Lunar farside volcanism 2.8 billion years ago from Chang'e-6 basalts. *Nature*, *643*(8071), 356–360. https://doi.org/10.1038/s41586-024-08382-0

Zhang, Y., Dasgupta, R., Ji, D., Lee, C.-T. A., Peng, Y., Charlier, B., et al. (2025). Mantle melting conditions of mare lavas on South Pole–Aitken basin of lunar farside. *Geophysical Research Letters*, *52*(6), e2024GL112418. https://doi.org/10.1029/2024gl112418

Zhao, Y., de Vries, J., van den Berg, A. P., Jacobs, M. H. G., & van Westrenen, W. (2019). The participation of ilmenite-bearing cumulates in lunar mantle overturn. *Earth and Planetary Science Letters*, *511*, 1–11. https://doi.org/10.1016/j.epsl.2019.01.022

Zhou, Q., Yang, W., Chu, Z., Zhu, H., Yang, S., Zeng, X., et al. (2025). Ultra-depleted mantle source of basalts from the South Pole–Aitken basin. *Nature*, *643*(8071), 371–375. https://doi.org/10.1038/s41586-025-09131-7

Zong, K., Wang, Z., Li, J., He, Q., Li, Y., Becker, H., et al. (2022). Bulk compositions of the Chang'E-5 lunar soil: Insights into chemical homogeneity, exotic addition, and origin of landing site basalts. *Geochimica et Cosmochimica Acta*, *335*, 284–296. https://doi.org/10.1016/j.gca.2022.06.037